Science Advances
AAAS

advances.sciencemag.org/cgi/content/full/5/8/eaav7913/DC1

Supplementary Materials for

Cranial endocast of a stem platyrrhine primate and ancestral brain conditions in anthropoids

Xijun Ni*, John J. Flynn, André R. Wyss, Chi Zhang

*Corresponding author. Email: nixijun@ivpp.ac.cn

Published 21 August 2019, *Sci. Adv.* **5**, eaav7913 (2019)
DOI: 10.1126/sciadv.aav7913

The PDF file includes:

Other Supplementary Material for this manuscript includes the following:

(available at advances.sciencemag.org/cgi/content/full/5/8/eaav7913/DC1)

Data file S1. Data matrix used for phylogenetic analysis (in NEXUS format).
Data file S2 (.nex format). MrBayes commands used for Bayesian tip dating analysis.
Data file S3 (Microsoft Word format). Fossil age, estimated divergence times, and branch length of selected fossil anthropoids.
Data file S4 (.tre format). The composite phylogenetic tree with estimated divergence times in NEXUS format.
Data file S5 (Microsoft Word format). Body mass and brain weight of extant and fossil haplorhine primates.
Data file S6 (Microsoft Word format). Regressions for ln(brain mass) and ln(body mass) in anthropoids, catarrhines, and platyrrhines.
Data file S7 (Microsoft Word format). PEQ, body mass, optic foramen area, orbital area, OFI, relative optic foramen size, and relative orbital size of extant and fossil haplorhine primates.
Data file S8 (Microsoft Word format). Regressions used for estimating acuity of the visual sensory system and the olfactory sensory system.
Data file S9 (Microsoft Word format). Body mass, brain mass, PEQ, olfactory bulb mass, and relative olfactory bulb size of extant and fossil haplorhine primates.

Phylogenetic analysis based on phenetic and molecular characters

To determine the phylogenetic position of *Chilecebus carrascoensis*, we ran a phylogenetic analysis built on a data matrix updated and modified from Ni et al. (*15*). This data matrix includes 1844 morphological and molecular characters, including 473 dental, 201 cranial, 309 postcranial, and 203 soft tissue features, as well as 658 molecular short and long interspersed nuclear elements (SINEs and LINEs) coded as present/absent. Only the haplorhine taxa of Ni et al.'s data matrix were included in the current analysis, given its focus on anthropoid brain evolution. We scored 10 additional key fossil platyrrhines and stem anthropoids in the data matrix: *Afrotarsius chatrathi*, *A. libycus*, *Soriacebus ameghinorum*, *Mohanamico hershkovitzi*, *Stirtonia tatacoensis*, *Neosaimiri fieldsi*, *Laventiana annectens*, *Killikaike blacki*, *Aotus dindensis* and *Chilecebus carrascoensis*. In total, 60 haplorhines are included in the analysis, *Tarsius syrichta* serving as the outgroup. Of the 1844 characters examined, 515 are invariant, and 938 are parsimony-informative. Of the 60 haplorhine taxa, 17 are extant platyrrhine, representing all the extant genera, and 12 extinct platyrrhine species.

The data matrix was edited in Mesquite v3.51 software (*36*) and saved in the NEXUS format (Data file S1). Specimens examined in scoring, and character descriptions are listed as notes in the NEXUS file.

We use both Bayesian and parsimony-based methods to infer the phylogeny. We applied Bayesian tip-dating to infer the tree topology and divergence times while accounting for their uncertainties. The analysis was carried out using MrBayes 3.2.7 (*37*)

The characters were divided into four partitions according to their anatomical and molecular affiliations, that is, dental (473 characters), cranial (201 characters), postcranial (309 characters), and

soft tissue and molecular (861 characters). The Mkv substitution model (*38*) was used for all characters. 944 characters were defined as ordered (see Data file S2), which means instantaneous change is only allowed between adjacent states, the rest of the characters were thus unordered. Evolutionary rate variations across characters and among partitions were both accommodated. The former was modelled under a discrete gamma distribution with mean 1.0 (*39*), while the latter was modelled under a uniform Dirichlet distribution (*40*).

The uniform tree prior (*41*) was used for the dating analysis. The root age was assigned a uniform prior between 56.67 and 66 Ma. The only known possible primate of modern aspect, *Altiatlasius koulchii*, from Paleocene of Morocco has an age estimation younger than 56.67 Ma (*42*). The rise of placental mammals, including primates, probably occurred after the Mesozoic extinction about 66 Ma (*43*). Each fossil age was assigned a uniform prior with lower and upper bounds from the corresponding stratigraphic range (see Data file S2). The relationships of extant taxa derived from a molecular super-matrix, i.e., a concatenation of 69 nuclear gene segments and 10 mitochondrial gene sequences covering 367 primate species across 70 genera (*35*), were used as a phylogenetic backbone. The soft tissue and SINE/LINE characters, which were scored for the extant taxa only, will not contribute to topology of the extant taxa because of the constraints, but including these characters provides useful branch length information and significantly shortens the convergence time of runs in the Bayesian inference analyses in MrBayes. The backbone scaffold also narrowed the tree space that MCMC could sample and helped with faster convergence and better mixing. *Tarsius syrichta* was defined as the outgroup to root the tree properly. The independent gamma (white noise) relaxed clock model (*44*) was applied for the evolutionary rate heterogeneity along the tree. The prior for the mean clock rate was gamma (2, 200) with mean 0.01, and that for the variance parameter was exponential (*35*).

We executed two independent runs with eight chains per run (one cold and seven heated with temperature parameter 0.05) for 30 million iterations and sampled every 1000 iterations. The first 30% samples were discarded as burn-in for each run. Sample consistency between runs was checked according to the average standard deviation of split frequencies (ASDSF) smaller than 0.01 (*45*) and the trace plots using Tracer (*46*). The samples from the two runs were combined to summarize the posterior estimates. The effective sample sizes (ESS) for all parameters were confirmed larger than 100.

MrBayes commands are available in the Data file S2. Tree topology and divergence times of the results are shown in fig. S1.

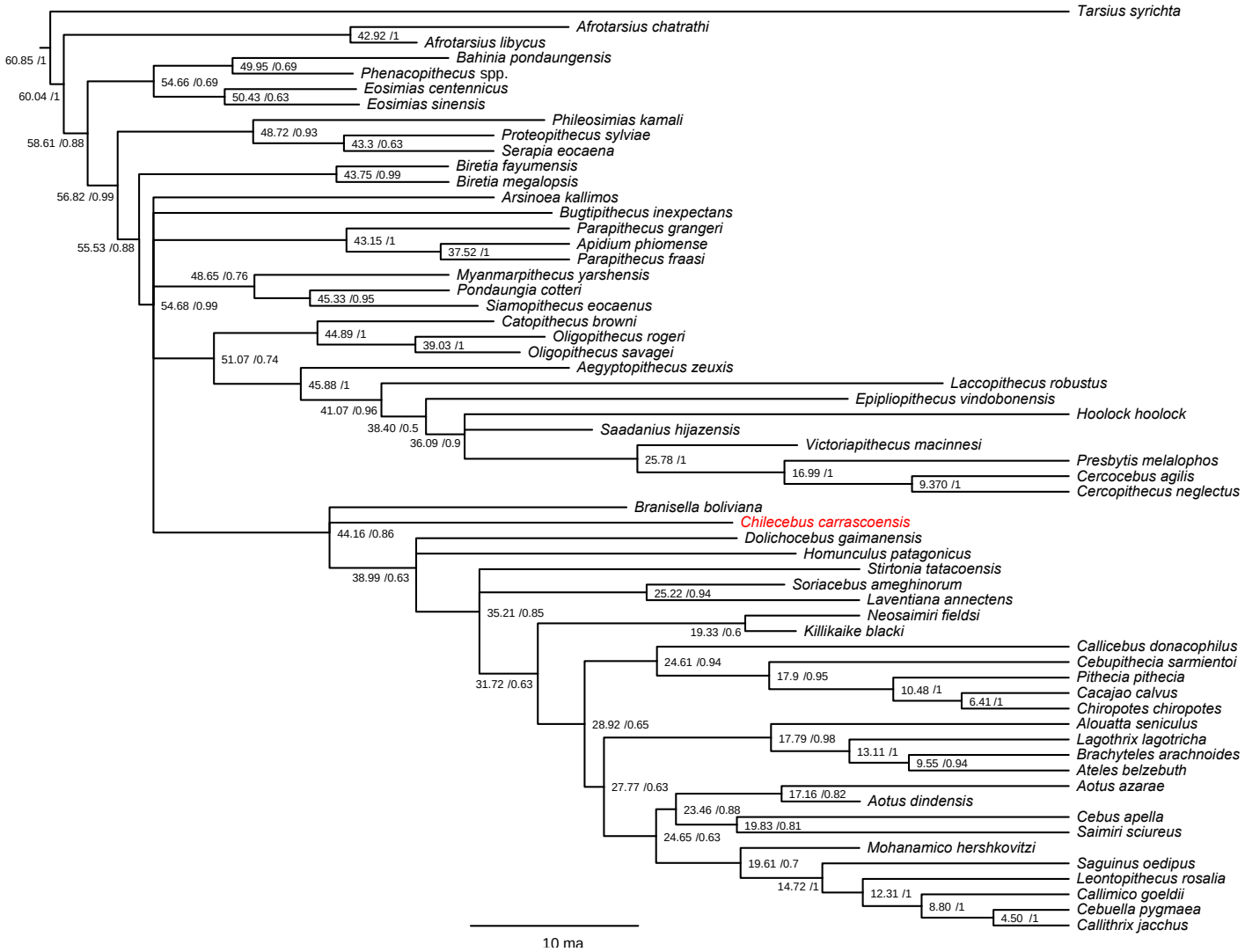

Fig. S1. Tree topology and divergence times of anthropoids inferred from Bayesian tip dating.

Bayesian inference is based on a data matrix including 1186 morphological characters and 658 molecular characters of long and short interspersed nuclear elements scored for 60 fossil and living haplorhines. Topology of extant primates, from a phylogeny based on a gene supermatrix (*35*), is used as backbone constraint. The number ahead of a slash at the internal node indicates the divergence time estimation. The number after a slash at the internal node indicates the posterior probability.

MrBayes commands are available in the Data file S2. Tree topology and divergence times of the results are shown in fig. S1.

Parsimony analysis of the total evidence dataset (dental, cranial, postcranial, soft tissue, LINE and SINE molecular data) was undertaken using TNT (Tree analysis using New Technology), a parsimony analysis program subsidized by the Willi Hennig Society (47). Search parameters used in identifying the most parsimonious trees follow the protocol of Ni et al. (15). The data matrix, in NEXUS format, was exported to TNT format. We ran multiple replications, using sectorial searches, drifting, ratchet and fusing combined searching strategy. Random sectorial search, constraint sectorial search, and exclusive sectorial search were activated. Ten cycles of tree drifting, 10 cycles of ratchet and 10 cycles of tree fusing were performed in the search. Default parameter settings for random sectorial search, constraint sectorial search, exclusive sectorial search, tree drifting, ratchet and fusing were used. The search level was set as 10 for 157 taxa. Optimal scores were hit 100 times independently, each hit with 100 initial replications (therefore 10000 replications in total). Some characters were run as ordered. All characters were assigned equal weight. The relationships of extant taxa derived from a molecular super-matrix (35) was used as a backbone constraint. The soft tissue and SINE/LINE characters increase the supports for the clades including extant taxa.

We used Bremer Supports and Relative Bremer Supports (*48*, *49*), calculated in TNT, to assess the stability of the phylogenetic result. The parameter setting follows the protocol of Ni et al. (*15*).

It required about 3 hours to run the parsimony analysis in TNT. In total, 39,577,479,738 rearrangements were examined. Six most parsimonious trees, each 4812 steps long, were retained. The

consistency index (CI) and retention index (RI) of the most parsimonious trees are 0.3478 and 0.6316 respectively. Results suggest that crown catarrhines and crown platyrrhines are both monophyletic groups. Extant platyrrhines and fossil stem platyrrhines also comprise a monophyletic group (fig. S2, S3), with high support (Bremer Decay Index of 5). *Chilecebus carrascoensis, Branisella boliviana* and *Dolichocebus gaimanensis* are three most basal taxa in the platyrrhine clade, also with high support for exclusion of these three taxa from the more crownward clade (Bremer Decay Index of 2). In the strict consensus tree, it is equally parsimonious to regard *Chilecebus*, *Branisella,* or *Dolichocebus* as the most basal platyrrhine, but the majority-rule consensus tree suggests that *Chilecebus* is the most basal of the three. Thus, *Chilecebus* is either the most basal or one of the three most basal known platyrrhines, and thus of great importance for constraining and understanding brain evolution both within this clade and in anthropoids more generally. This result is generally consistent with a recent, independent study (*50*) based on a smaller dataset, which includes 399 dental characters and osteological features of the cranium and postcranium scored for 16 extant and 20 extinct taxa of platyrrhines.

Fig. S2. Strict consensus of six most parsimonious phylogenetic trees. Parsimony analysis was performed in TNT, based on a data matrix including 1186 morphological characters and 658 molecular characters of long and short interspersed nuclear elements scored for 60 fossil and living haplorhines. Topology of extant primates, from a phylogeny based on a gene supermatrix (*35*), is used as backbone constraint. Numbers at the internal nodes of the tree are Bremer Decay Index nodal support scores (before the slashes) and Relative Bremer Decay Index nodal support scores (after the slashes) (*48*).

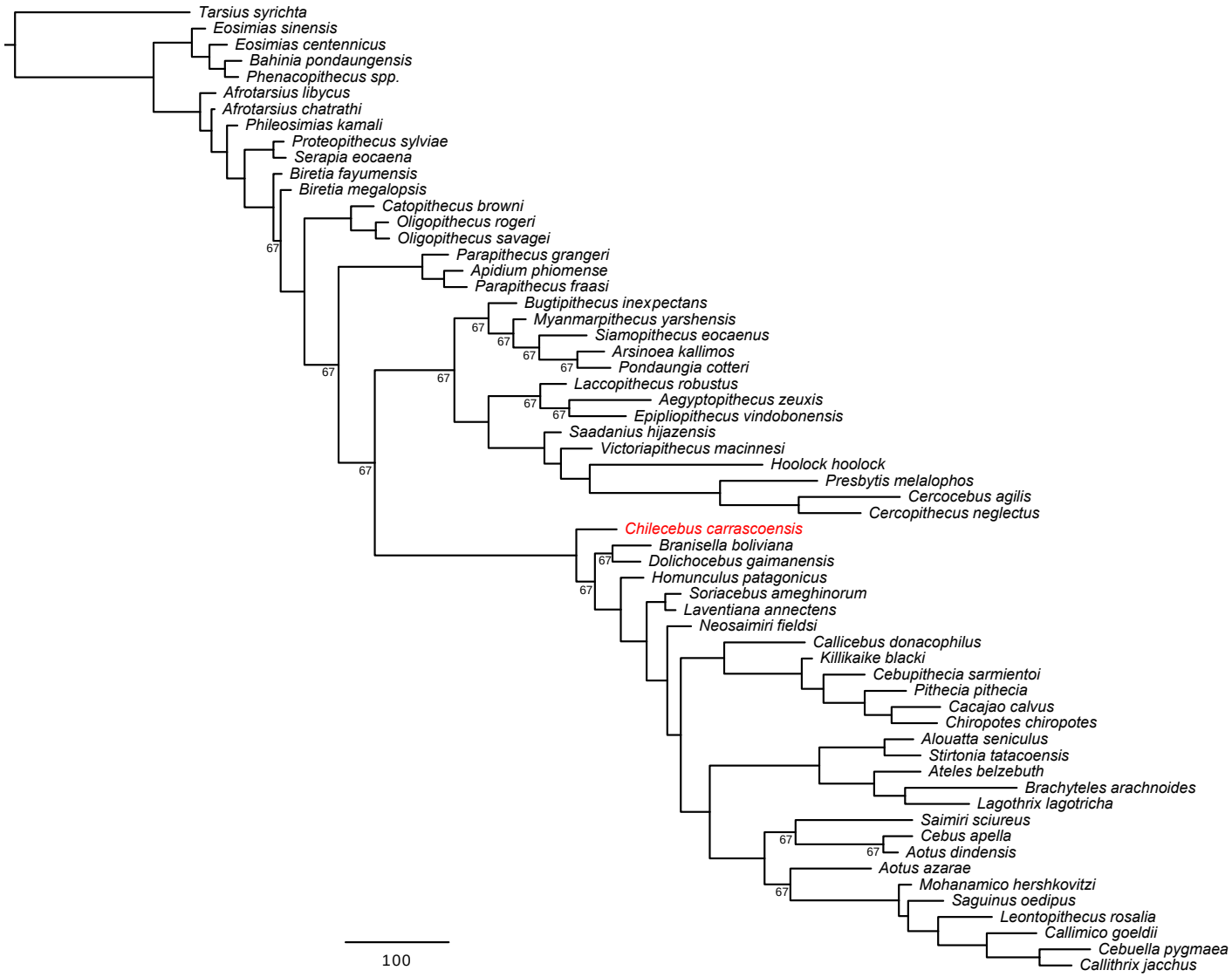

Fig. S3. Majority consensus of six most parsimonious phylogenetic trees. Parsimony analysis was performed in TNT, based on a data matrix including 1186 morphological characters and 658 molecular characters of long and short interspersed nuclear elements scored for 60 fossil and living haplorhines. Topology of extant primates, from a phylogeny based on a gene supermatrix (*35*), is used as backbone constraint. Numbers at internal nodes of the tree are the percentage of occurrences among the equally parsimonious trees in the consensus phylogeny. Internal nodes without number are the ones with 100% occurrence in the consensus tree.

The Bayesian inferred and parsimony phylogenetic trees show some differences, but both support *Chilecebus* as a stem platyrrhines, and platyrrhines and catarrhines as monophyletic groups.

Composite phylogenetic tree and estimated divergence times

Our Bayesian phylogenetic tree, based on phenotypic characters and SINE and LINE genetic markers, was combined with the molecular phylogenetic tree based on Springer et al.'s gene super-matrix (*35*) and the consensus hominid phylogenetic tree based on phenomic characters (*51*). Only the fossil taxa preserving the skulls and having the endocasts reconstructed were incorporated into Springer et al.'s super tree. The phylogenetic positions of *Proteopithecus*, *Parapithecus*, *Chilecebus*, *Homunculus*, *Catopithecus*, *Aegyptopithecus* and *Victoriapithecus* relative to extant species are based on our Bayesian analysis. The position of *Anapithecus* is estimated from the positions of *Laccopithecus* and *Epipliopithecus* in the Bayesian analysis. The phylogenetic position of *Dryopithecus* is still debatable. Here we followed a wide accepted systematic placement of *Dryopithecus* as the basal member of Hominidae (*52*). Taxa without endocranial volume data were trimmed from the statistic and character maping analyses.

The divergence times of lineages leading to extant species are from Springer et al.'s molecular timetree with autocorrelated rates and soft-bounded constraints (*35*). The divergence time of a given fossil species is estimated as the mean of the time of the previous and subsequent nodes of this species in the composite phylogenetic tree, or the Bayesian estimation (Data file S3). The branch length of the fossil taxon is calculated as the difference between the estimated divergence time and the fossil's age. The data in the "Data file S3" are from this research and the references (*11, 53-65*).

The composite phylogenetic tree with estimated divergence times in NEXUS format is provided in Data file S4.

Virtual endocranial cast of *C. carrascoensis*

fig. S4 illustrates the virtual endocranial cast of Chilecebus based on high-resolution x-ray CT scanning images. The views and labels correspond to those of Fig. 1 in the main text.

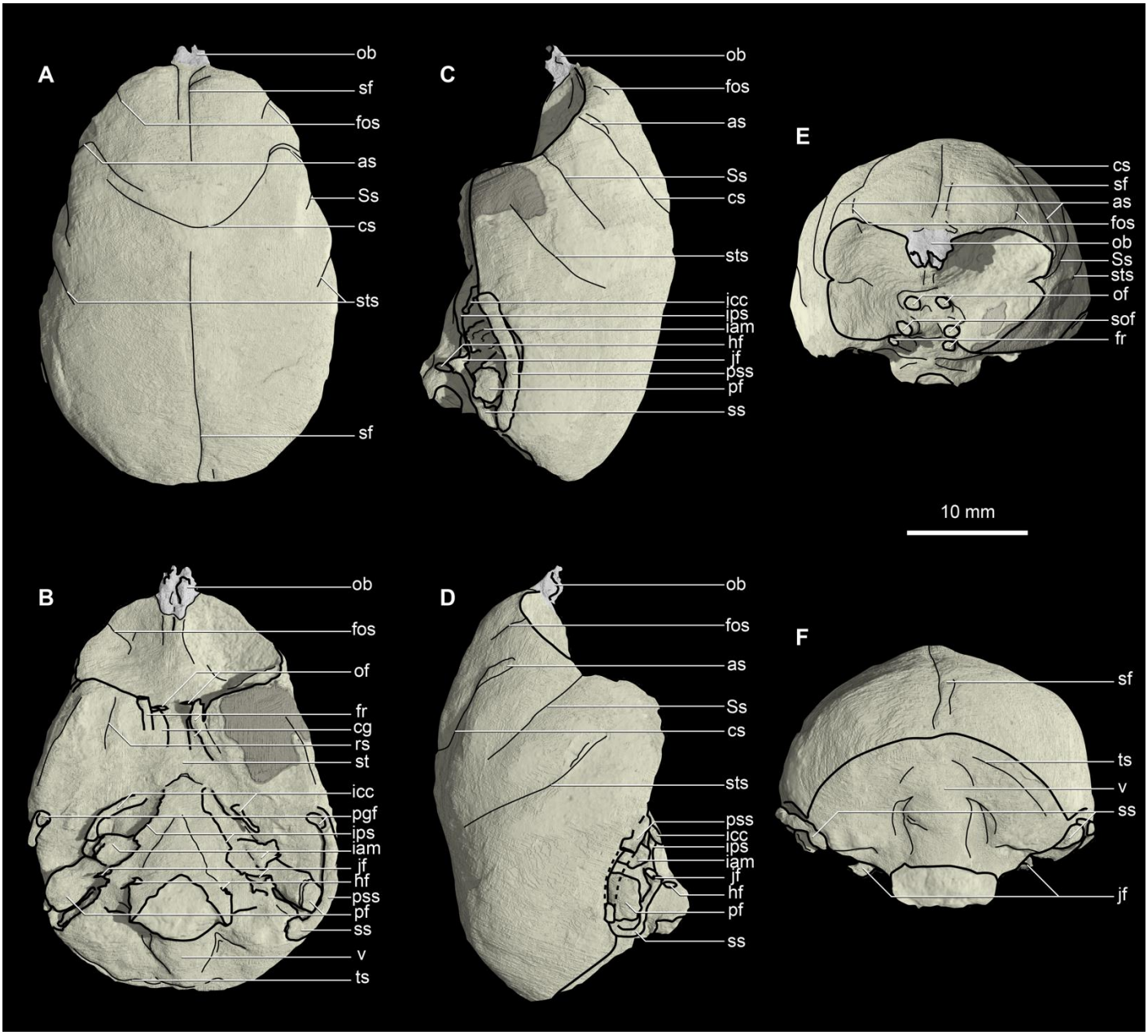

Fig. S4. Virtual endocranial cast of *C. carrascoensis* based on high-resolution x-ray CT scanning images. Grey shadows indicate reconstructed portions. A. dorsal; B. ventral; C. left lateral; D. right lateral; E. anterior; F. Posterior. Abbreviation: *as*, arcuate sulcus; *cg*, cavernous groove; *cs*, central sulcus; *fos*, fronto-orbital sulcus; *fr*, foramen rotundum; *hf*, hypoglossal foramen; *iam*, internal acoustic meatus; *icc*, internal carotid canal; *ips*, inferior petrosal sinus; *jf*, jugular foramen; *ob*, olfactory bulb; *of*, optic foramen; *pf*, paraflocculus; *pgf*, postglenoid foramen; *pss*, petrosquamous sinus; *rs*, rhinal sulcus;

sf, sagittal fissure; *sof*, superior orbital fissure; *Ss*, Sylvian sulcus; *ss*, sigmoid sinus; *st*, sella turcica; *sts*, superior temporal sulcus; *ts*, transverse sulcus; *v*, vermis.

Measurements of the virtual endocranial cast of *C. carrascoensis*

Measurements of the virtual endocranial cast of *Chilecebus carrascoensis* are listed in Table S1.

Table S1. Measurements of the virtual endocranial cast of *C. carrascoensis* [mm, mm^2 (areas), or mm^3 (volumes)].

Item	Measurements
Endocranial volume	7682.00
Nasion-opisthocranion length	34.12
Porion-porion width	25.90
Frontal lobe width	20.33
Frontal lobe sagital length	15.42
Temporal-temporal width	17.37
Medulla oblongata width at the foramen magnum	8.70
Medulla oblongata thickness at the foramen magnum	6.04
Pons width	6.23
Cerebellar width from posterior view	20.97
Cerebellar width at the flocculus	23.74
Cerebellar thickness from posterior view	7.50
Vermis width from posterior view	6.52
Olfactory bulb width	3.37

Olfactory bulb length	3.48
Olfactory bulb volume	11.10
Optic foramen length	1.78
Optic foramen width	1.12
Optic foramen area	1.57

Comparison of lateral profiles of endocranial casts

The lateral profile of the virtual endocranial cast of *Chilecebus* was compared with those of fossil and extant anthropoids: *Aegyptopithecus zeuxis* (stem catarrhine), *Dolichocebus gaimanensis* (stem platyrrhine), and four representative extant platyrrhines with small and larger body and brain sizes (*Callithrix pygmaea*, *Callithrix jacchus*, *Saguinus imperator* and *Saimiri sciureus*) (fig. S5). Compared pairs were aligned along a line connecting the nasion and opisthocranion, and then rescaled to the same nasion-opisthocranion length.

Chilecebus and *Dolichocebus* show very similar lateral profiles although the brain of *Dolichocebus* is much larger absolutely than that of *Chilecebus*. The ventral side of the temporal lobe of *Dolicocebus* is not exposed, but it has been reconstructed based on the outer surface of the skull (*1*). The temporal lobes of both taxa are similar in relative size. The posterior part of the frontal lobe, and the parietal lobe, of *Dolichocebus* are slightly more dorsally expanded than in *Chilecebus*. However, because the skull of *Dolichocebus* is compressed bi-laterally, it is uncertain whether this difference simply reflects post-mortem deformation.

Extant callitrichines and *Chilecebus* have similar nasion-opisthocranion lengths. The temporal lobe of *Chilecebus* relative to its nasion-opisthocranion lengh is larger than those of extant callitrichines, but the latter all show more significant dorsal expansion than *Chilecebus*. *Callithrix pygmaea* has the smallest absolute brain mass among extant anthropoids. In lateral profile, its frontal pole is slightly expanded compared to *Chilecebus*. The occipital and the temporal lobes of *Chilecebus* are broader than those of *C. pygmaea.* The parietal lobe of the latter is greatly expanded dorsally relative to *Chilecebus*. In *Chilecebus* the portion of the brain above the nasion-opisthocranion axis is smaller than the portion below the axis, whereas in *C. pygmaea* this relationship is reversed. The brains of *Callithrix jacchus* and *Chilecebus* are very similar in lateral profile. The frontal, occipital and temporal lobes of both taxa match very well in shape and proportions, but *C. jacchus* differs in its slightly more dorsally expanded cortex. The parietal lobe of *C. jacchus* shows similar depression as in *Chilecebus* and *Dolichocebus*. In *Saguinus,* the portion of the brain above the nasion-opisthocranion axis is much larger than that below the axis, indicating significant dorsal expansion relative to other parts of the brain.

Extant platyrrhines with larger absolute and relative brain sizes, here taking *Saimiri* as an example, have more greatly expanded frontal, parietal and occipital lobes than *Chilecebus*. Their temporal lobes, however, are much smaller (relatively) than in *Chilecebus*.

The lateral profile of *Aegyptopithecus*, a basal catarrhine, differs strikingly from that of *Chilecebus*. Its temporal lobe is much smaller proportionally (relative to its nasion-opisthocranion lengh) than in *Chilecebus*, and its frontal lobe is more dorsally expanded. The occipital lobe of *Aegyptopithecus,* proportionally extremely small, does not overlap the cerebellum, whereas the occipital lobe of *Chilecebus* well overlaps the cerebellum dorsally and laterally.

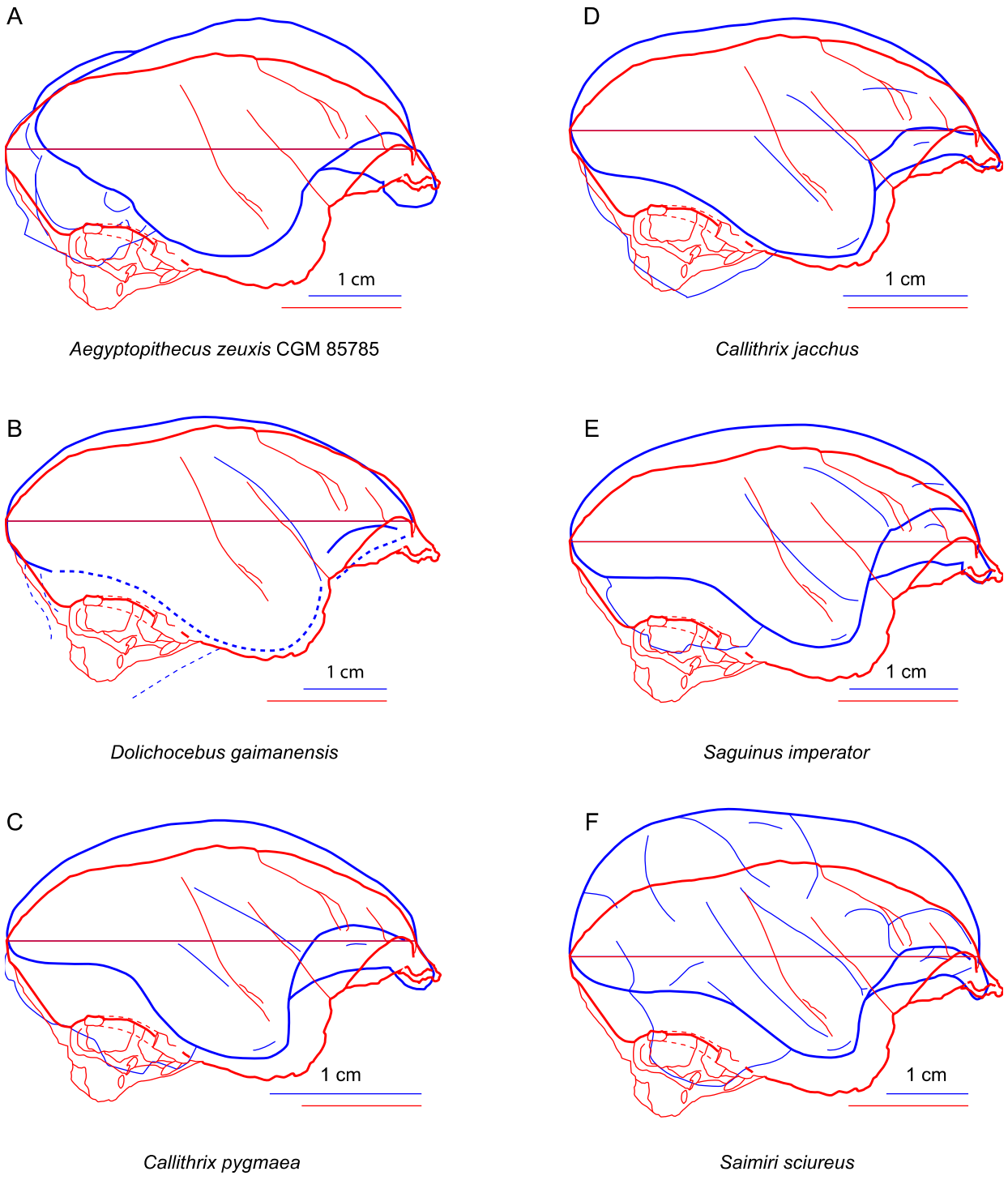

Fig. S5. Comparison of the lateral profile of the endocranial cast of *C. carrascoensis* with other anthropoids. A. With *Aegyptopithecus zeuxis*; B. With *Dolichocebus gaimanensis*; C. With *Callithrix pygmaea*; E. With *Callithrix jacchus*; F. With *Saguinus imperator*; G. With *Saimiri sciureus*. The red

lines show *Chilecebus*, blue lines the taxa being compared. The red scale bar is for *Chilecebus*, the blue scale bar for the comparison taxon.

Allometric relationship between brain and body mass

Endocranial volumes and body masses (Data file S5) of extant and fossil anthropoids, except *Chilecebus*, were collected from publications (*1, 16, 17, 25, 55, 56, 58, 60, 62, 64-79*). Brain mass is estimated from the endocranial volume, by assuming a density of fresh brain tissue of 1.036g/cc (*73*). We used the "ape" and "nlme" packages for R 3.5.1 (*80*) to analyze the data. Models for calculating phylogenetic correlation structures in "ape" and the fitting functions of "nlme" are powerful and flexible for analyzing phenotypic character evolution (*20*). We created a correlation structure assuming a Brownian motion model, by using the corBrownian function of "ape;" a correlation structure was subsequently used to fit the linear model in "nlme". The composite phylogenetic tree was used to generate the phylogenetic correlation structures. Only the data for extant anthropoids were used for generating Phylogenetic Generalized Least Squares (PGLS) and Generalized Least Squares (GLS) regressions. The results of PGLS analyses are listed in Data file S6.

To test for the significance of the differences between the *ln*(brain mass)-*ln*(body mass) PGLS regressions of platyrrhines and catarrhines, we combined the catarrhine and platyrrhine data, and introduced a dummy variable Grp. Let Grp equal 1 when a taxon is a platyrrhine, and let Grp equal 0 when a taxon is a catarrhine. We used the model: *ln*(brain mass)~ Grp + *ln*(body mass)+ *ln*(body mass):Grp, with the corBrownian correlation structure. The variable Grp tests the null hypothesis Ho: $b_{catarrhine} = b_{platyrrhine}$. The variable *ln*(body mass):Grp tests the null hypothesis Ho: $a_{catarrhine} = a_{platyrrhine}$.

Here neither of the variables is significant, suggesting that the PGLS regression for platyrrhines and the PGLS regression for catarrhines do not differ statistically (Data file S6).

Tracing PEQs along the composite phylogenetic tree

The PEQ, phylogenetic encephalization quotient, calculated from the PGLS regression, is a novel index of relative brain size. We used maximum likelihood estimation and Bayesian inference to reconstruct the ancestral states and to trace the changes of PEQs along the composite phylogenetic tree by using the contMap and anc.Bayes commands of the Phytools package of R (*81*) . A full version of the result is shown in fig. S6.

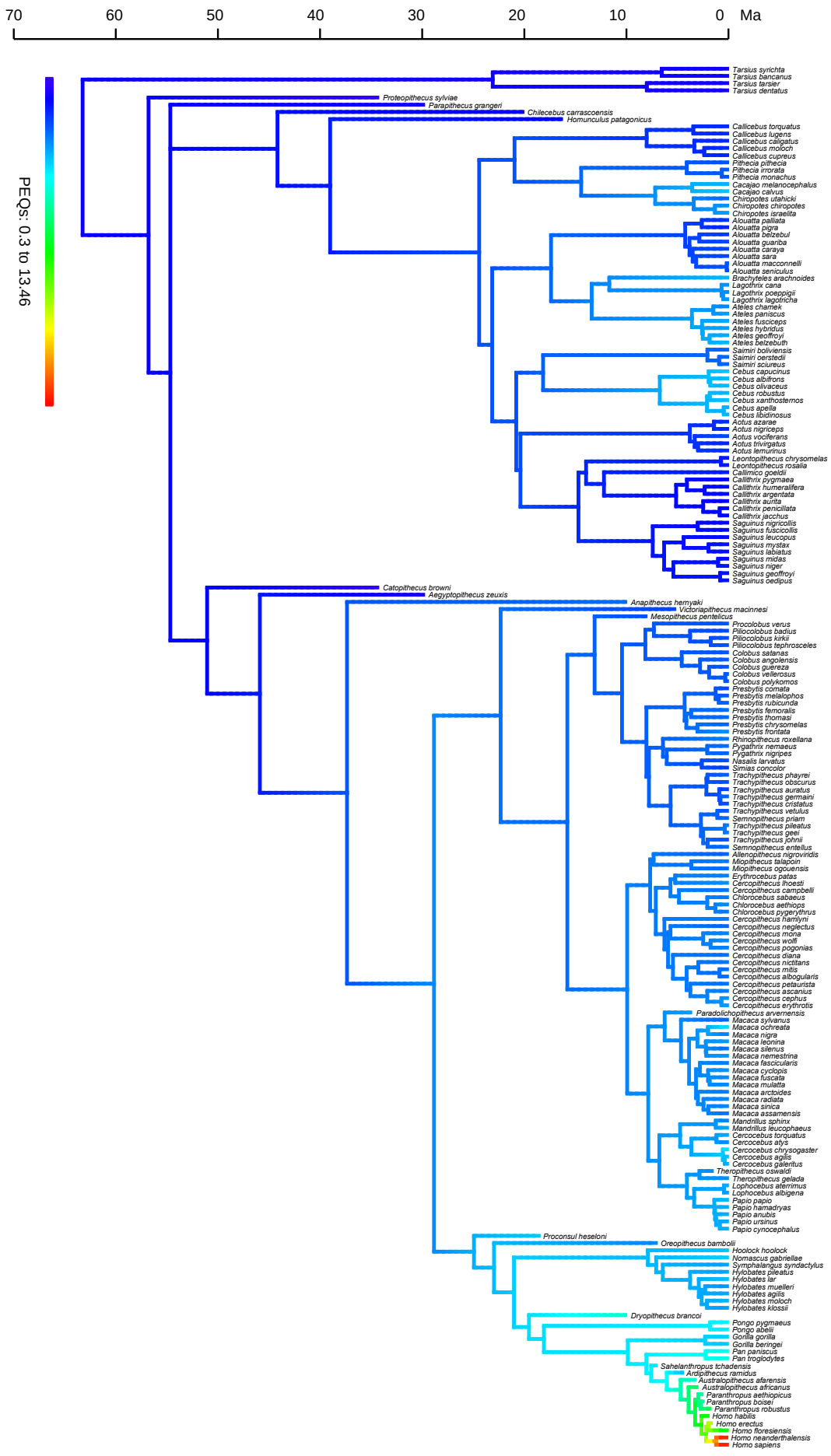
70
60
50
40
30
20
10
0
Ma
PEQs: 0.3 to 13.46
Tarsius syrichta
Tarsius bancanus
Tarsius tarsier
Tarsius dentatus
Proteopithecus sylviae
Parapithecus grangeri
Chilecebus carrascoensis
Homunculus patagonicus
Callicebus torquatus
Callicebus lugens
Callicebus caligatus
Callicebus moloch
Callicebus cupreus
Pithecia pithecia
Pithecia irrorata
Pithecia monachus
Cacajao melanocephalus
Cacajao calvus
Chiropotes utahicki
Chiropotes chiropotes
Chiropotes israelita
Alouatta palliata
Alouatta pigra
Alouatta belzebul
Alouatta guariba
Alouatta caraya
Alouatta sara
Alouatta macconnelli
Alouatta seniculus
Brachyteles arachnoides
Lagothrix cana
Lagothrix poeppigii
Lagothrix lagotricha
Ateles chamek
Ateles paniscus
Ateles fusciceps
Ateles hybridus
Ateles geoffroyi
Ateles belzebuth
Saimiri boliviensis
Saimiri oerstedii
Saimiri sciureus
Cebus capucinus
Cebus albifrons
Cebus olivaceus
Cebus robustus
Cebus xanthosternos
Cebus apella
Cebus libidinosus
Aotus azarae
Aotus nigriceps
Aotus vociferans
Aotus trivirgatus
Aotus lemurinus
Leontopithecus chrysomelas
Leontopithecus rosalia
Callimico goeldii
Callithrix pygmaea
Callithrix humeralifera
Callithrix argentata
Callithrix aurita
Callithrix penicillata
Callithrix jacchus
Saguinus nigricollis
Saguinus fuscicollis
Saguinus leucopus
Saguinus mystax
Saguinus labiatus
Saguinus midas
Saguinus niger
Saguinus geoffroyi
Saguinus oedipus
Catopithecus browni
Aegyptopithecus zeuxis
Anapithecus hernyaki
Victoriapithecus macinnesi
Mesopithecus pentelicus
Procolobus verus
Piliocolobus badius
Piliocolobus kirkii
Piliocolobus tephrosceles
Colobus satanas
Colobus angolensis
Colobus guereza
Colobus vellerosus
Colobus polykomos
Presbytis comata
Presbytis melalophos
Presbytis rubicunda
Presbytis femoralis
Presbytis thomasi
Presbytis chrysomelas
Presbytis frontata
Rhinopithecus roxellana
Pygathrix nemaeus
Pygathrix nigripes
Nasalis larvatus
Simias concolor
Trachypithecus phayrei
Trachypithecus obscurus
Trachypithecus auratus
Trachypithecus germaini
Trachypithecus cristatus
Trachypithecus vetulus
Semnopithecus priam
Trachypithecus pileatus
Trachypithecus geei
Trachypithecus johnii
Semnopithecus entellus
Allenopithecus nigroviridis
Miopithecus talapoin
Miopithecus ogouensis
Erythrocebus patas
Cercopithecus lhoesti
Cercopithecus campbelli
Chlorocebus sabaeus
Chlorocebus aethiops
Chlorocebus pygerythrus
Cercopithecus hamlyni
Cercopithecus neglectus
Cercopithecus mona
Cercopithecus wolfi
Cercopithecus pogonias
Cercopithecus diana
Cercopithecus nictitans
Cercopithecus mitis
Cercopithecus albogularis
Cercopithecus petaurista
Cercopithecus ascanius
Cercopithecus cephus
Cercopithecus erythrotis
Paradolichopithecus arvernensis
Macaca sylvanus
Macaca ochreata
Macaca nigra
Macaca leonina
Macaca silenus
Macaca nemestrina
Macaca fascicularis
Macaca cyclopis
Macaca fuscata
Macaca mulatta
Macaca arctoides
Macaca radiata
Macaca sinica
Macaca assamensis
Mandrillus sphinx
Mandrillus leucophaeus
Cercocebus torquatus
Cercocebus atys
Cercocebus chrysogaster
Cercocebus agilis
Cercocebus galeritus
Theropithecus oswaldi
Theropithecus gelada
Lophocebus aterrimus
Lophocebus albigena
Papio papio
Papio hamadryas
Papio anubis
Papio ursinus
Papio cynocephalus
Proconsul heseloni
Oreopithecus bambolii
Hoolock hoolock
Nomascus gabriellae
Symphalangus syndactylus
Hylobates pileatus
Hylobates lar
Hylobates muelleri
Hylobates agilis
Hylobates moloch
Hylobates klossii
Dryopithecus brancoi
Pongo pygmaeus
Pongo abelii
Gorilla gorilla
Gorilla beringei
Pan paniscus
Pan troglodytes
Sahelanthropus tchadensis
Ardipithecus ramidus
Australopithecus afarensis
Australopithecus africanus
Paranthropus aethiopicus
Paranthropus boisei
Paranthropus robustus
Homo habilis
Homo erectus
Homo floresiensis
Homo neanderthalensis
Homo sapiens

Fig. S6. Tracing PEQs along the composite phylogenetic tree of fossil and extant haplorhine primates (data file S4). Ancestral states were reconstructed by using maximum likelihood estimation and Bayesian inference.

Estimating acuity of the visual sensory system

The optic foramen index (OFI) was calculated as the quotient of dividing orbital area by optic foramen area (*22*). We analyzed the allometric relationships of the optic foramen and orbital size against body mass by using the "ape" and "nlme" packages of R 3.5.1 (*20, 80*). PGLS regressions for *ln*(optic foramen area) and *ln*(body mass) and for *ln*(orbital area) and *ln*(body mass) were calculated with correlation structures assuming a Brownian motion model. The composite phylogenetic tree was used for calculating correlation structures. Data are in Data file S7, which are collected from the publications (*22, 25, 79*). Both regressions are significant (Data file S8).

The relative optic foramen size was calculated by dividing the observed optic foramen area by the expected optic foramen calculated from the PGLS regression for *ln*(optic foramen area) and *ln*(body mass). The relative orbital size was calculated by dividing the observed orbital area by the expected orbital area calculated from the PGLS regression for *ln*(orbital area) and *ln*(body mass). Relative optic foramen and relative orbital foramen measures thus remove the effect of body mass.

We tested the relationship between PEQs and relative optic foramen size, relative orbital size, and OFI respectively by using PGLS analyses. We excluded *Homo sapiens* from the analysis, because its PEQ is vastly higher than that of all other haplorhines. Relative optic foramen size and relative orbital size are

significantly linearly correlated with PEQs (Data file S8), but the relationship between PEQs and OFI is not significant (Data file S8).

Estimating acuity of the olfactory sensory system

The olfactory bulb masses of extant haplorhines are collected from the publication (*82*) and listed in Data file S9. Only the data of extant primates were used for analyzing the allometric relationship between olfactory bulb and body mass and between olfactory bulb and brain mass. As in the analyses for estimating acuity of visual sensory system, we used PGLS regression analysis with correlation structures assuming a Brownian motion model. Relative olfactory bulb size was calculated by dividing the observed olfactory bulb mass by the olfactory bulb mass expected based on the PGLS regression for *ln*(olfactory bulb mass) and *ln*(body mass). The relative size of the olfactory bulb in fossil anthropoids was calculated by using the PGLS regression equation derived from extant haplorhines.

Olfactory bulb mass shows significant allometric relationships with body and brain mass (Data file S8). Relative olfactory bulb size, which removes the body mass scaling effect, shows considerable variation among extant and fossil haplorhines. Although the olfactory bulb of *Chilecebus* is small for an animal of its size, it falls within the variation range exhibited by extant anthropoids (fig. S6). Relative olfactory bulb size is not significantly correlated with PEQs in haplorhines (Data file S8).

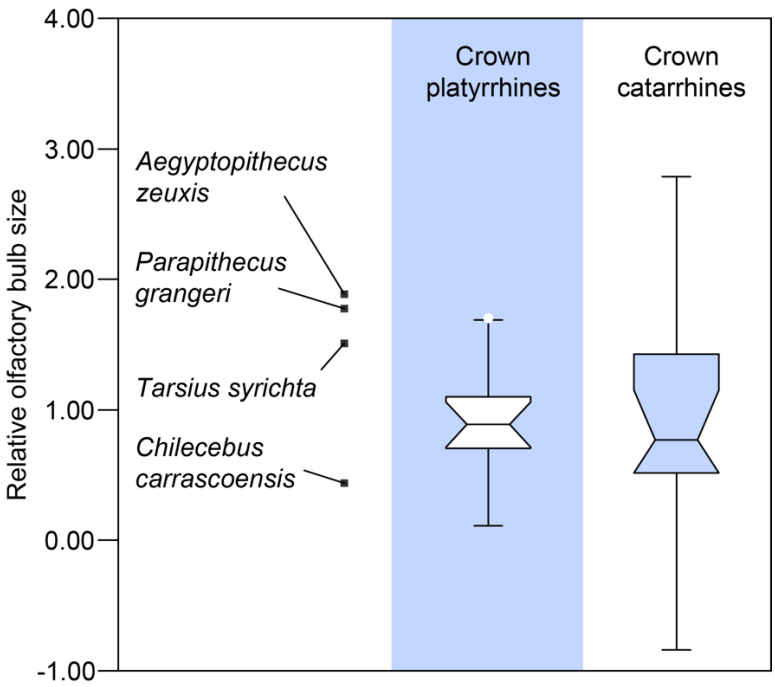

Fig. S7. Notched box-whisker plot of the relative olfactory bulb size of fossil and extant haplorhine primates. Whiskers show the lowest datum within 1.5 interquartile range (IQR) of the lower quartile, and the highest datum still within 1.5 IQR of the upper quartile. Outliers are shown as circles.

Olfactory bulb size is correlated with ecological factors among extant primates (*24*, *83*, *84*), particularly to nocturnal versus diurnal activity patterns and diet. Diurnal primates tend to have smaller olfactory bulbs than nocturnal forms, while frugivorous and insectivorous taxa have larger olfactory bulbs than folivorous taxa (independent of activity pattern). Since a diurnal activity pattern can be inferred for *Chilecebus* from the its relatively small orbit and optic foramen and higher OFI than nocturnal haplorhines (main text Fig. 4), its relatively small olfactory bulb is suggestive of a folivorous diet. The dental morphology of *Chilecebus* is consistent with a frugivorous or folivorous diet (*11*). Given the recently revised estimates of its body mass, however, *Chilecebus* was more likely folivorous (*12*, *67*), consistent with new and independent (non-dental, non-body mass) data presented here.

References

References are listed in the main text.

Captions for additional file types that cannot be embedded into this file

Data file S1. Data matrix used for phylogenetic analysis (in NEXUS format).

Data file S2. MrBayes commands used for Bayesian tip dating analysis.

Data file S3. Fossil age, estimated divergence times, and branch length of selected fossil anthropoids.

Data file S4. The composite phylogenetic tree with estimated divergence times in NEXUS format.

Data file S5. Body mass and brain weight of extant and fossil haplorhine primates.

Data file S6. Regressions for ln(brain mass) and ln(body mass) in anthropoids, catarrhines, and platyrrhines.

Data file S7. PEQ, body mass, optic foramen area, orbital area, OFI, relative optic foramen size, and relative orbital size of extant and fossil haplorhine primates.

Data file S8. Regressions used for estimating acuity of the visual sensory system and the olfactory sensory system.

Data file S9. Body mass, brain mass, PEQ, olfactory bulb mass, and relative olfactory bulb size of extant and fossil haplorhine primates.